Design and fabrication of bimetallic plasmonic colloids through cold nanowelding

Mariacristina Turino, Enrique Carbó-Argibay, Miguel Correa-Duarte, Luca Guerrini, Nicolas Pazos-Perez and Ramon A. Alvarez-Puebla

Abstract

Integration of Au and Ag into nanoalloys has emerged as an intriguing strategy to further tailor and boost the plasmonic properties of optical substrates. Conventional approaches to fabricate these materials via chemical reductions of metal salts in solution suffer from some limitations, such as the possibility of retaining the original morphology of the monometallic substrate. Spontaneous nanowelding at room temperature has emerged as an alternative route to tailor Au/Ag nanomaterials. Herein, we perform a thorough study on the cold-welding process of silver nanoparticles onto gold substrates to gain a better understanding of the role of different variables in enabling the formation of well-defined bimetallic structures that retain the original gold substrate morphology. To this end, we systematically varied the silver nanoparticles size, gold substrate dimensions and geometries, solvent polarity and structural nature of the polymeric coating. A wide range of optical and microscopy techniques have been used to provide a complementary and detailed description of the nanowelding process. We believe this extensive study will provide valuable insights into the optimal design and engineering of bimetallic plasmonic Ag/Au structures for application in nanodevices.

Introduction

Metal nanoparticles, mostly made of gold and silver, have emerged as a unique tool to control light–matter interactions at the nanoscale, which is driven by the generation of collective oscillations known as localized surface plasmon resonances (LSPRs).1 LSPRs can also lead to the concentration of extremely high electromagnetic (EM) energies at the nanostructured plasmonic surfaces which, in turn, can couple with EM fields emitted by molecules located in their proximity. This promotes striking effects which have been exploited in different plasmonic-enhanced spectroscopies, most notably in surface-enhanced Raman spectroscopy (SERS).1, 2 Overall, nanoplasmonic applications extend across multidisciplinary areas such as biotechnology,3, 4 photovoltaics,5 nanocatalysis,6 and nanomedicine.7, 8

As the optical response of plasmonic nanoparticles is strictly dependent on their size, shape, composition and geometrical arrangement, the ability to synthetically produce a la carte nanomaterials with well-defined, homogeneous and robust architecture is central to their efficient technological implementation. Plasmonic nanostructures are preferably made with Ag and Au, thanks to the good metallic properties and low absorption of these two materials. While silver typically provides better optical efficiency over a broader spectral range, gold commonly enables higher control over the size and shape of the fabricated nanoparticles.9, 10 Notably, combining Au and Ag into bimetallic nanomaterials has emerged as a valuable route to further tailor the plasmonic properties of the substrates.11-13 Several approaches have been developed to the fabrication of such Ag/Au materials, which are mostly based on chemical reductions in solution.11-13 This strategy, while being relatively simple and low-cost, does suffer from some limitations. In particular, for a controlled overgrowth on top of another metallic colloidal

surface, it is required that the surface free energy of the metal to be reduced must be lower than the metallic colloids otherwise a galvanic replacement will occur instead.14, 15 For the case of Au and Ag, the surface free energy of Ag (0.923 Jm-2) is lower than for Au (1.128 Jm-2)16 and, therefore, a layer of Ag can be easily grown onto AuNPs by redox reactions.17, 18 However, this growth is selective for specific crystallographic planes.19 Thus, the heterogeneous distribution of crystallographic planes on the nanoparticles causes asymmetric growth of the coating metal, thus hampering the possibility of retaining the original particle morphology.20

On the other hand, it is known that when two metallic NPs come into contact, they spontaneously coalesce. This solid-state process, known as cold-welding, occurs by the transport of atoms via atomic diffusion and surface relaxation to reduce the surface free energy. Indeed, at the nanoscale, the diffusion barrier for a single metal atom on a clean metal surface is very low (ca. 1.0 eV),21 thus permitting the nanowelding process to proceed at room temperature.22, 23 During this process, the fusion of NPs is thermodynamically driven (spontaneous) and represents a common phenomenon observed in colloidal systems (referred to as Ostwald ripening) in which smaller particles coalesce to form larger particles.24 Such phenomenon has emerged as an attractive way for bottom-up assembly at the nanoscale.25-28

Herein, we performed a thorough study on the cold-welding of small spherical silver nanoparticles (AgNPs) over a diverse range of gold nanomaterials of various sizes and shapes to yield bimetallic structures retaining the original gold substrate morphologies. This was achieved regardless of their initial features via a homogeneous silver coating. Notably, we highlighted key parameters that affect the evolution of the nanowelding process, such as AgNPs diameter, AgNPs surface density, solvent polarity, and Au nanostructure geometrical features (e.g., surface curvature). Surface-enhanced Raman spectroscopy (SERS) was also used as an efficient characterization tool for monitoring nanowelding, an application of this technique that has been largely underexploited so far.29, 30

Materials and methods

Materials

Tetrachloroauric acid (≥99%, $HAuCl_4 \cdot 3H_2O$), trisodium citrate dihydrate (≥99.5%, $C_6H_5Na_3O_7 \cdot 2H_2O$), ascorbic acid (99%, $C_6H_8O_6$), silver nitrate (99,8%, $AgNO_3$), n-hexane (≥99.5%, C_6H_{14}), chloroform (≥99%, $CHCl_3$), and oleylamine (90%, OA) were acquired from Acros Organics. Triisopropylsilane (98%, TIPS) was purchased from Alfa Aesar. Branched polyethyleneimine (≥99.5%, PEI), iron nitrate nonahydrate (≥99.5%, $FeN_3O_9 \cdot 9H_2O$), cetyltrimethylammonium bromide (99.72%, CTAB), and sodium borohydride (99%, $NaBH_4$), poly(allylamine hydrochloride) (PAH, molecular weight = 17.5 k), poly(diallyldimethylammonium chloride) solution 20 wt. % in H_2O (PDDA, medium molecular weight = 200-350 k), were purchased from Sigma-Aldrich. Ethanol was acquired from Scharlab (≥99%, C_2H_5OH). All reactants were used without further purification. Milli-Q water (18 MΩ cm−1) was used in all aqueous solutions. All glassware was cleaned with aqua regia before use.

Synthesis of ultrathin gold nanowires

0.4 mL of OA was mixed with 12 mg of HAuCl4 in 10 mL of hexane followed by the addition of 0.6 mL TIPS. The mixture was left reacting undisturbed overnight at room temperature. The mixture turns into a brownish color due to the formation of the thin Au nanowires. Next, the nanowires were cleaned by centrifugation (one time at 4000 rpm, 4 min) after the addition of 20 mL of ethanol. The final precipitate was redispersed in 10 mL of chloroform.31, 32

Assembly of nanowires in bundles and PEI wrapping

The obtained wires were mixed with 8 mL of a PEI solution in chloroform (0.01 g per 10 mL). The mixture was left overnight until flocculation occurs. Then, it was centrifuged twice (4000 rpm, 4 min) and the pellet was redispersed in 20 mL of ethanol and stored. Prior the welding process to assure that all the chloroform was removed from the solution and that the nanowires were fully coated with PEI, 500 µL of the assembled nanowires were added dropwise to an ethanol solution of PEI (0.02 g/10 mL). After two hours in the stirring wheel, the sample was centrifuged twice (4000 rpm, 4 min). The so obtained positively charged bundles were redispersed in 500 µL of water.

Synthesis of spherical silver nanoparticles (ca. 33 and 43 nm diameter)

33 nm size AgNPs were prepared by adding a mixture containing AA (100 µL, 0.1 M) and C6H5Na3O7·2H2O (600 µL, 0.1 M) to a 100 mL of boiling water under vigorous stirring. 1 minute later, a solution previously incubated for 5 min containing AgNO3 (198 µL, 0.1 M) and FeN3O9·9H2O (22 µL, 0.001 M) was also added.33 Boiling and stirring were continued for 1 h. The samples were concentrated by solvent evaporation until reaching a final Ag0 concentration of 10-3 M. The obtained NPs diameter was 33 ± 3 nm. To produce AgNPs of 43 ± 4 nm size, the same protocol was applied but the amounts of the reagents were adjusted as follows. A mixture of AA (100 µL, 0.1 M) and C6H5Na3O7·2H2O (908 µL, 0.1 M) was added to 100 ml of boiling water under vigorous stirring. After 1 minute, AgNO3 (298 µL, 0.1 M) was also injected. The colloidal suspension was concentrated to [Ag0] = 10-3 M.

Synthesis of CTAB-stabilized gold nanorods and PEI wrapping

Gold nanorods of high aspect ratios were produced adapting a previously published seed-mediated method.34-36 Briefly, gold seeds were synthesized by adding to 5 mL of water, 12,75 µL of C6H5Na3O7·2H2O 0.1 M. Then 12.18 µL of HAuCl4 0.1 M were also added under vigorous stirring. Next, a freshly prepared solution of NaBH4 (150 µL, 0.1 M) was quickly injected, and the color of the solution immediately changes from light yellow to red. The mixture was left under energetically stirring for 1h in an open atmosphere to ensure complete decomposition of NaBH4. Then, a growth solution was prepared by dissolving 9.111 g of CTAB in 250 mL of water. To the latter, 1.218 mL of HAuCl4 0.1 M were mixed and gently shaken until complete dissolution. The solution color turned from orange to transparent upon injection of 1.837 mL of AA 0.1 M. After that, 500 µL of seeds were carefully added into the foam of the growth solution and the mixture was left undisturbed for 24 h at 27 °C. During this time, the high aspect ratio nanorods sediment and can be separated from the supernatant containing mainly spheres. The collected pellet was redispersed in 20 mL of water and washed two times more by sedimentation to maximize the removal of spherical NPs. Finally, the cleaned rods were redispersed in 40 mL of an aqueous CTAB solution 0.1 M. To increase the particle width of the Au rods, a second seeding-growth step was carried out using the obtained nanorods as seeds. A new

growth solution was prepared by adding to 20 mL of CTAB 0.1 M, 24.36 µL of HAuCl4 0.1 M. Once completely dissolution of the gold salt, 73.5 µL of AA 0.1 M were injected and 100 µL of nanorods previously synthesized were introduced in the foam of the solution. After vigorously shaking, the growth mixture was let undisturbed overnight. The, grown nanorods were washed twice by centrifugation and stored in CTAB 0.1 M for further use (length: 1085 ± 114 nm; width: 94 ± 15 nm). To wrap the nanorods with PEI, 500 µL of the overgrown nanorods, were added dropwise to 5 mL of a PEI solution (2 mg/mL) under vigorous stirring. After 3 hours, the mixture was washed once, the pellet was redispersed in 500 µL of water and added again drop by drop to 5 mL of PEI solution (2 mg/mL). The mixture was left overnight under stirring to ensure the complete surfactant-polymer exchange. After that, particles were washed five times and finally redispersed in 1 mL of water.

Growth of CTAB-stabilized gold nanospheres and PEI wrapping

Gold nanospheres were grown starting from particles of 70 nm diameter as seeds. To 10 mL of CTAB 0.1 M, 48.72 µL of HAuCl4 0.1 M were added. Once completely dissolved, 73.5 µL of AA 0.1 M were injected. Then, 600 µL and 4.8 mL of gold nanospheres (70 nm size). The solutions were vigorously shaken and left undisturbed overnight. The pellet was collected, washed twice (2000 rpm, 5 min), and finally redispersed in 10 mL of CTAB 0.1 M. Monodisperse spheroidal gold particles of 107 ± 6 nm and 199 ± 9 nm were obtained, respectively.36 For the polyelectrolyte wrapping, 1 mL of both nanospheres was washed twice and mixed with 5 mL of a PEI solution (2 mg/mL) under vigorous magnetic stirring. The mixtures were left overnight under stirring. Nanospheres were then washed five times by centrifugation (2000 rpm, 5 min) and finally redispersed in 1 mL of water.

Synthesis of small spherical silver nanoparticles (ca. 15 nm diameter)

Spherical Ag nanoparticles of approx. 15 nm diameter were synthesized adding to 100 mL of boiling water, a mixture containing AA (100 µL, 0.1 M) and sodium citrate (600 µL, 0.1 M) under vigorous magnetic stirring. After 1 min, a solution incubated for 5 minutes containing 198 µL of AgNO3 0.1 M and 79 µL of Fe(NO3)3 0.01 M was also added. The color turns from transparent to dark red and finally to bright yellow.33 After 1 h, the samples were concentrated by solvent evaporation until reaching a final Ag0 concentration of 10-3 M. The NPs size was 15 ± 2 nm.

Assembly of spherical Ag nanoparticles onto PEI coated NPs

Au bundles were coated with Ag nanoparticles (ca. 33 and 43 nm diameters) by the dropwise addition of 500 µL of the PEI-covered nanowires to 5 mL of Ag colloids. Nanoparticle suspensions were previously washed once. The mixtures were left overnight and washed one time with water to remove the excess of unbound Ag NPs. Finally, the core-satellites assemblies were redispersed in 1.5 mL of water or 1.5 mL of ethanol for TEM and UV-Vis characterization. Small AgNPs were assembled onto gold nanorods and gold spheres in a similar manner. 1 mL of PEI wrapped gold NPs were added dropwise and under sonication to 5 mL of 15 nm size AgNPs solutions (previously washed once). The core-satellites nanostructures were left to sediment and the recovered pellet was washed once with water and finally redisperse in 1 mL of water for storage and further characterization.35

SERS characterization

Samples for SERS characterization were prepared as follows. 50 µL of colloidal suspensions (i.e., individual Au cores and Ag satellites, or the assembled core-satellites composites at different stages of the welding process) were deposited onto a previously RCA cleaned glass slide and spin coated ((1st ramp) 500 rpm, 10 s; (2nd ramp) 3000 rpm, 30 s, with an acceleration rate of 500 rpm s−1 for both ramps). This is to assure that SERS measurements were performed on individual structures. Finally, the materials were exposed to benzenethiol in gas phase (overnight incubation).

Instrumentation

Transmission electron microscopy (TEM) images were acquired by using a JEOL 1011 operating at 80 kV and a FEI Titan Themis Cubed (Probe- and Image-corrected TEM) operating at 200 kV was used to analyze the elemental composition of the particles by energy-dispersive X-ray (EDX) spectroscopy. Extinction spectra were recorded using a Thermo Scientific Evolution 201 UV-visible spectrophotometer. SERS measurements were performed using a Renishaw InVia Reflex confocal microscope equipped with high-resolution gratings (2400 or 1200 grooves per cm for the visible or NIR, respectively) with additional band-pass filter optics, a confocal microscope and a 2D-CCD camera. 514, 633, and 785 nm laser lines were focused on the sample through a ×50 objective with the acquisition time of 10 s and the power at the sample of about 2.6 mW. The provided spatial resolution was ca. 1 µm obtaining SERS maps under the same conditions in an area of 50 × 50 µm.

Results and discussion

Cold-welding technology involving ultrathin metallic nanowires (NWs) has been intensively investigated in recent years as a valuable tool to promote nanojoining processes for designing nanodevices.27, 37-39 Thus, we initiated our study using this class of materials by fabricating ca. 1.6 nm diameter Au nanowires (NWs) according to our previously described protocol.32 In a subsequent step, the ultrathin structures (Fig. 1A and Fig. S1) were functionalized with PEI promoting the extensive formation of heterogeneous bundles of wires as illustrated in Fig. 1B and Fig. S1. NWs self-assembly into close-packed bundles is commonly used to prevent structural fragmentation.40 The PEI functionalization allows the transfer of the wires to aqueous solution while imparting positive charge. In fact, change in surface charge is required to promote the subsequent adhesion of negatively charged citrate-capped silver nanoparticles of 33 ± 3 nm (AgNP33, Fig. 1C and Fig. S2) to yield the corresponding bundle@AgNP33 materials (Fig. 1D and Fig. S3). After 1 day upon the assembly, NWs and NPs appear as well-separated in independent units (Fig. 1D). After 4 days, however, nanoparticles appear to begin merging with the Au bundles (Fig. 1E) which became more prominent at day 7 (Fig. 1F) then, after 11 days, the silver structures are almost completely integrated into the wire support, though their semispherical shapes can still be clearly distinguished (Fig. 1G). Three days later (Fig. 1H), metallic silver has been fully embedded within the bundles, leading to the formation of a thicker wire favored by the atomic diffusion of silver along the gold surfaces. After this period, the structure does not show any visible alteration (Fig. 1I).

Scanning transmission electron microscopy (STEM) combined with spectroscopic mapping by energy dispersive X-ray (EDX) spectroscopy was also performed on representative bundle@AgNP33 to monitor the elemental distribution during the cold-welding process (Fig. 2). The elemental maps visualize the distribution of protruding

spherical-like areas of Ag along a linear Au backbone at day 4. As the process continues (from day 7 onward), the bulging areas of high Ag density, as well as the residual interparticle gaps, progressively disappear, as the Ag incorporation into the bundle structure advances. Past 14 days of the initial assembly, Ag and Au are homogeneously distributed over the whole structure which resembles a core/shell structure (Au@Ag) with segregation of both elements as depicted from the line scan analysis shown in Fig. S4. The qualitative information extracted from the TEM images and STEM-EDX characterization is mirrored by the optical interrogation of the whole ensemble of bundle@AgNP33 in suspension. The normalized extinction spectra displayed in Fig. 1J show that after the initial assembly, the optical response is dominated by the feature at ca. 405 nm, assigned to the contribution of individual nanoparticle LSPRs with minimal interparticle coupling. After 4 days, this plasmonic feature undergoes significant broadening and drop in intensity, consistently with the reshaping of the surface-bound AgNPs. As a result, the weak contribution at 520 nm, associated with the LSPRs of the Au bundles, gains prominence in the spectral profile. The optical changes after day 4 are, however, very subtle, which can be related to the complex and heterogeneous bundle geometries which difficult the discrimination of cold-welded induced structural changes.

Overall, these data demonstrate that AgNPs act as the soft matter that "wets" the hard gold surface by the movement of Ag atoms over the bundle surface at room temperature, which is also the reason why the gold structure retains its original morphology upon merging.25 On the other hand, it has been previously reported that welding of two NPs of similar size and shape that came into physical contact selectively occurs through a common lattice plane, which is an indication of an oriented attachment.27, 41 Indeed, nanoparticles, differently from nanowires and nanofilms, can freely rotate to adjust the lattice structure which, in turn, paves the way for the natural cold welding process to occur.42 In the specific case of cold welding between the NWs bundles and AgNPs, both materials have similar face center cubic lattice (FCC) arrangements with lattice parameters of 4.08 Å for Au and 4.09 Å for Ag,26 showing inter-fringe distances of 0.23 nm and 0.24 nm. This corresponds to the (111) lattice spacing for both types of materials.27 Thus, the joint between Au bundles and AgNPs takes place via an oriented attachment mechanism as previously described,27 where the AgNPs align through an atom-by-atom rearrangement of their crystallographic planes.

Remarkably, when transferred to ethanol, bundles@AgNP33 assemblies exhibit minimal signs of silver nanoparticles welding onto the gold surfaces even after 14 days (Fig. S5). This phenomenon may be correlated to the reduction in solvent polarity when using ethanol in place of water. In fact, lowering the solvent polarity has been associated with a decrease in diffusion and solvation.43 To investigate the role of AgNPs size on the merging with gold bundles, nanoparticles of ca. 10 nm larger in diameter (43 ± 4 nm, Fig. S6) were fabricated to generate the corresponding bundle@AgNP43 composite materials. Surprisingly, we observed that such an apparently small increase in nanoparticle size has a tremendous impact on the kinetic of the welding process. Indeed, even after 30 days, the 43 nm size AgNPs, while interconnected, still maintained a pseudo spherical shape resembling "pearls necklaces" (Fig. S7) with no smoothing along the bundles of Au wires. This result clearly highlights the key role of AgNPs size in controlling the evolution of the welding and, thus, the homogeneous coating of the gold counterpart.

Based on these results, we decided to continue our study on the welding process of AgNPs onto gold nanostructures by using (i) 15 ± 2 nm diameter silver nanoparticles (AgNP15, Fig. S8) as the smallest, colloidally stable and homogeneous citrate-capped AgNPs currently available,33 and (ii) uniform long Au nanorods (AuNRs). On the one hand, reducing the AgNPs size is expected to significantly fasten the merging process. On the other, we replace a structurally heterogeneous gold material, such as the bundles, with uniform penta-twined long AuNRs of ca. 94 nm width and ca. 1 μm in length (Fig. S9) to acquire a clearer view of the process. As for bundles, AuNRs were wrapped with a PEI layer to trigger the electrostatic accumulation of AgNP15 onto nanorods and the generation of the corresponding NR@AgNP15 materials. Representative TEM images acquired at different moments after the initial assembling (30 min, 1h, 3h, 6h,1 day, 2 days and 6 days) are illustrated in Fig. 3A-G and Fig. S10. The dense collection of AgNP15 on AuNRs begins to display indications of nanoparticle reshaping after just 1h (Fig. 3B). At 3h total time (Fig. 3C), the extension of the welding process becomes more evident, as nanoparticles start merging and forming a continuous layer on the NR surfaces. At this stage, the welding process is largely completed although a flat and smooth silver coating is only achieved after approximately 4 days (Fig. 3F,G). This second stage of the process, driven by atomic diffusion along the side of the rods, exhibits lower kinetics as compared to the initial NPs merging. In this case, the monitoring of the optical properties of the well-defined NR@AgNP15 materials during the welding process provides a clearer picture of the structural reshaping (Fig. 3H) as compared to the bundle@AgNPs composites. At 30 min, the NR@AgNP15 assemblies display two distinct peaks centered at ca. 400 nm and 660 nm. The former is ascribed to the LSPR of AgNPs (Fig. 3I) while the latter is assigned to the transversal mode of the NRs which is, however, redshifted as compared to the original AuNRs (535 nm) due to the plasmon coupling with AgNPs. As expected, as the welding proceeds, we observe the progressive redshift and intensity decrease of Ag contribution until its full disappearance at day 1, due to NP merging. This is mirrored by the transversal NR contribution undergoing a continuous blueshift until ca. 525 nm (day 4), when the formation of a smooth Ag layer is completed. It is to note that such transversal plasmon mode does not reach the value of the pristine AuNRs, in agreement with what was observed for shorter silver-coated gold nanorods obtained via chemical reduction of silver salts.13

NRs exhibit two different crystallographic planes at their surface: a five-fold cross-section made up of {111} facets and five {100} facets which ran the length of the NRs.34, 44, 45 Meanwhile, the AgNPs are multi-twinned particles with {111} facets facing the NRs surface. As seen from the TEM images in Fig. 3, welding occurs at both crystallographic planes of the NRs. At the tips, the AgNPs and AuNRs bound mainly through {111} facets whereas the welding along the rod length takes place between the {100} facets of the rods and the {111} facets of the AgNPs. The fact that it has not been observed any appreciable difference in the welding between the tips and the sides of the NRs suggests that a non-crystallographic selective process has occurred.

Both bundle@AgNPs and NR@AgNP15 assemblies were fabricated using branched PEI as polymeric coating for gold substrates. Different positively charged polyelectrolytes (poly(allylamine hydrochloride), PAH; and poly(diallyldimethylammonium chloride), PDDA) were also tested. However, the resulting NR@AgNP15 exhibited a lower surface density of silver nanoparticles (Fig. S11). In these cases, though a welding phenomenon did occur (Fig. S11), it developed into an inhomogeneous distribution of Ag along the NRs

surfaces via an apparently slower process. This is most likely associated with the increased separation between surface-bound AgNPs that hampers the fast atomic diffusion.

In the next step of our study, we examined the role of the geometrical features of the Au substrate. In this regard, we transitioned from long rods to spherical AuNPs with a diameter approximately equal to the NRs thickness (i.e., the dimensions of the gold substrate were maintained in the xz plane with the reduction of the NR length to match the sphere diameter). Thus, 107 ± 6 nm size AuNPs (Fig. 4A and S12) were first coated with PEI and then combined with AgNP15 to yield the corresponding AuNP107@AgNP15 core-satellites. Representative TEM images of the AuNP107 and the corresponding assemblies at different aging times (1, 4, 8, 12, and 20 days) are illustrated in Fig. 4A-F and Fig. S13. Differently from NRs, after 4 days most of the AgNPs on Au spheres still retain a spherical morphology, and the welding process remains far to be completed (Fig. 4C). Approximately 8 days are necessary to discern a plain loss of Ag nanoparticles geometry (Fig. 4D) and ca. 20 days to observe the almost complete fusion onto the Au substrate, though bulging Ag spots can be still distinguished (Fig. 4F). These results are in agreement with the time evolution UV-Vis spectral analysis reported in Fig. 4G. On day 1, the LSPRs of individual Au and AgNPs shift from 580 nm and 400 to 670 nm and 430 nm, respectively, due to plasmon coupling. After 4 days, the two plasmon resonances became broader but remain mainly centered at the same positions, revealing that the welding process has been taking place at a relatively low rate. The blueshift of the Au feature as well as the overall drop in intensity and spectral broadening of both Ag and Au contributions are far more pronounced in the later days.

The welding process of AuNP107@AgNP15 assemblies was also monitored using surface-enhanced Raman spectroscopy (SERS). As a probe molecule, we selected benzenethiol (BT). The nanostructures, previously spin-coated on a glass slide, were exposed to a saturated atmosphere of BT in the gas phase to guarantee a full monolayer coating. SERS maps were recorded by interrogating the samples using three different lasers with excitation wavelengths of 514, 633 and 785 nm. Notably, only when illuminated with the NIR source, the samples provide intense SERS signals. The acquired SERS spectra reveal the characteristic spectral bands of BT centered at ca. 999 cm-1, ascribed to ring stretching, and 1020 and 1070 cm-1, assigned to C–H in-plane deformations (Fig. 5A).46 The detected intensity of the 1070 cm-1 band is represented at different stages of the welding process (Fig. 5B). For comparison, BT-coated AuNP100 and AgNP15 were also separately interrogated, but silver nanoparticles did not provide any detectable signal due to the weak enhancing capabilities of such small colloids. As it can be seen, SERS intensity undergoes an initial increase when AgNPs are assembled onto the Au core, which is associated with the formation of interparticle Ag-Ag and Au-Ag gaps. Based on our previous study on similar structures,35 the larger electromagnetic contribution to the SERS signal resides at the core-satellite gaps rather than emerging from the plasmon coupling between adjacent small satellite particles. This is consistent with the subsequent drop in intensity observed from day 1 to ca. day 7, when Ag nanoparticles progressively weld on top of the Au core. After day 8, there is a sudden rise in SERS intensity, reaching a plateau on day 9. This can be associated with the formation of a continuous silver layer on the gold core yielding nanoparticles analogous to conventional Au-core/Ag-shell obtained via chemical reduction, which have shown to display higher SERS activities as compared to the corresponding monometallic counterparts.47, 48

These results highlight the central role of the Au substrate geometrical features in shaping the evolution of the welding process. This appears directly correlated with the level of AgNPs surface density that, in turn, would increases as the gold support is progressively "flattened". To further corroborate this hypothesis, we replaced AuNP107 with nanospheres of smaller curvatures (i.e., larger nanoparticles with 199 ± 9 nm diameter, AuNP199, Fig. 6A and Fig. S14). Fig. 6B-D (Fig. S15) and Fig. 6E show representative TEM images and extinction spectra, respectively, of the AuNP199@AgNP15 composites after different days upon the initial assembling. Overall, the results demonstrate that much faster kinetics can be achieved by increasing the gold nanoparticle size. Indeed, representative TEM images show that a smooth and homogeneous layer of silver is obtained on day 6, indicating the full completion of the welding process (Fig. 6D). At this stage, the optical analysis reveals an extinction spectrum where the feature associated with AgNP15, initially centered at 400 nm, has largely disappeared due to nanoparticle fusion. On the other hand, the quadrupolar and dipolar contributions of AuNPs, respectively located at ca. 560 nm and 760 nm, remain visible although redshifted as compared to those of pristine gold particles (Fig. 6E).

Conclusions

In summary, we performed an extensive study on the nanowelding process of silver nanoparticles of increasing diameters onto gold substrates of diverse geometrical features to gain a better understanding of the role of different variables in enabling the formation of well-defined bimetallic structures that retain the original gold substrate morphology. To this end, we employed a wide array of techniques, including SERS spectroscopy as a powerful surface characterization tool. The formation of homogenous and smooth silver coating is favored by decreasing the silver nanoparticles size while maximizing their surface loading. This latter factor is strictly related to the nature of the polymeric coating of gold substrates, with PEI showing the best result, which is possibly related to its branched structure. On the other hand, a decrease in gold substrate dimensions (i.e., higher surface curvature) significantly slows the nanowelding process. We believe this extensive study provides valuable insights into the optimal design and engineering of bimetallic plasmonic Ag/Au structures for application in nanodevices.

Acknowledgements

This research was supported by the projects PID2020-120306RB-I00 and PID2020-113704RB-I00 (funded by MCIN/AEI/10.13039/501100011033), PDC2021-121787-I00 (funded by MCIN/AEI/10.13039/501100011033 and European Union Next Generation EU/PRTR), RYC-2016-20331 (funded by Spanish Ministerio de Economia y Competitividad), 2017SGR883 (funded by Generalitat de Cataluña) and 2021PFR-URV-B2-02 (funded by Universitat Rovira I Virgili). This project has received funding from the European Union's Horizon 2020 Research and Innovation Programme under the Marie Skłodowska-Curie grant agreement no. 713679 and from the Universitat Rovira i Virgili. Xunta de Galicia (Centro Singular de Investigación de Galicia - Accreditation 2019-2022 ED431G 2019/06, IN607A 2018/5 and ED431C 2021/45), and European Union-ERDF (Interreg V-A - Spain-Portugal 0245_IBEROS_1_E, 0712_ACUINANO_1_E, and 0624_2IQBIONEURO_6_E, and Interreg Atlantic Area NANOCULTURE 1.102.531). This work was carried out in part through the use of the INL User Facilities.

Notes and references

1. V. Giannini, A. I. Fernandez-Dominguez, S. C. Heck and S. A. Maier, Chem. Rev., 2011, 111, 3888-3912.

2. S. Schlücker, Angew. Chem.-Int. Edit., 2014, 53, 4756-4795.

3. B. Pelaz, C. Alexiou, R. A. Alvarez-Puebla, F. Alves, A. M. Andrews, S. Ashraf, L. P. Balogh, L. Ballerini, A. Bestetti, C. Brendel, S. Bosi, M. Carril, W. C. W. Chan, C. Chen, X. Chen, X. Chen, Z. Cheng, D. Cui, J. Du, C. Dullin, A. Escudero, N. Feliu, M. Gao, M. George, Y. Gogotsi, A. Grünweller, Z. Gu, N. J. Halas, N. Hampp, R. K. Hartmann, M. C. Hersam, P. Hunziker, J. Jian, X. Jiang, P. Jungebluth, P. Kadhiresan, K. Kataoka, A. Khademhosseini, J. Kopeček, N. A. Kotov, H. F. Krug, D. S. Lee, C.-M. Lehr, K. W. Leong, X.-J. Liang, M. Ling Lim, L. M. Liz-Marzán, X. Ma, P. Macchiarini, H. Meng, H. Möhwald, P. Mulvaney, A. E. Nel, S. Nie, P. Nordlander, T. Okano, J. Oliveira, T. H. Park, R. M. Penner, M. Prato, V. Puntes, V. M. Rotello, A. Samarakoon, R. E. Schaak, Y. Shen, S. Sjöqvist, A. G. Skirtach, M. G. Soliman, M. M. Stevens, H.-W. Sung, B. Z. Tang, R. Tietze, B. N. Udugama, J. S. VanEpps, T. Weil, P. S. Weiss, I. Willner, Y. Wu, L. Yang, Z. Yue, Q. Zhang, Q. Zhang, X.-E. Zhang, Y. Zhao, X. Zhou and W. J. Parak, ACS Nano, 2017, 11, 2313-2381.

4. I. Calderon, L. Guerrini and R. A. Alvarez-Puebla, Biosensors, 2021, 11, 230.

5. U. Aslam, V. G. Rao, S. Chavez and S. Linic, Nature Catalysis, 2018, 1, 656-665.

6. Y. C. Zhang, S. He, W. X. Guo, Y. Hu, J. W. Huang, J. R. Mulcahy and W. D. Wei, Chem. Rev., 2018, 118, 2927-2954.

7. L. Wang, M. H. Kafshgari and M. Meunier, Adv. Funct. Mater., 2020, 30, 28.

8. L. Guerrini, E. Garcia-Rico, A. O'Loghlen, V. Giannini and R. A. Alvarez-Puebla, Cancers, 2021, 13, 2179.

9. J. Zhao, A. O. Pinchuk, J. M. McMahon, S. Li, L. K. Ausman, A. L. Atkinson and G. C. Schatz, Acc. Chem. Res., 2008, 41, 1710-1720.

10. F. J. García de Abajo, Rev. Mod. Phys., 2007, 79, 1267-1290.

11. A. Sánchez-Iglesias, E. Carbó-Argibay, A. Glaria, B. Rodríguez-González, J. Pérez-Juste, I. Pastoriza-Santos and L. M. Liz-Marzán, Chem. Eur. J., 2010, 16, 5558-5563.

12. Liu and P. Guyot-Sionnest, The Journal of Physical Chemistry B, 2004, 108, 5882-5888.

13. M. Tebbe, C. Kuttner, M. Mayer, M. Maennel, N. Pazos-Perez, T. A. F. König and A. Fery, J. Phys. Chem. C, 2015, 119, 9513-9523.

14. Y. Sun, B. T. Mayers and Y. Xia, Nano Lett., 2002, 2, 481-485.

15. Y. Sun and Y. Xia, Science, 2002, 298, 2176-2179.

16. G. Guisbiers, R. Mendoza-Cruz, L. Bazán-Díaz, J. J. Velázquez-Salazar, R. Mendoza-Perez, J. A. Robledo-Torres, J.-L. Rodriguez-Lopez, J. M. Montejano-Carrizales, R. L. Whetten and M. José-Yacamán, ACS Nano, 2016, 10, 188-198.

17. M. Fernanda Cardinal, B. Rodríguez-González, R. A. Alvarez-Puebla, J. Pérez-Juste and L. M. Liz-Marzán, J. Phys. Chem. C, 2010, 114, 10417-10423.

18. D. Tsoutsi, J. M. Montenegro, F. Dommershausen, U. Koert, L. M. Liz-Marzán, W. J. Parak and R. A. Alvarez-Puebla, ACS Nano, 2011, 5, 7539-7546.

19. M. Mayer, L. Scarabelli, K. March, T. Altantzis, M. Tebbe, M. Kociak, S. Bals, F. J. García de Abajo, A. Fery and L. M. Liz-Marzán, Nano Letters, 2015, 15, 5427-5437.

20. S. Gómez-Graña, B. Goris, T. Altantzis, C. Fernández-López, E. Carbó-Argibay, A. Guerrero-Martínez, N. Almora-Barrios, N. López, I. Pastoriza-Santos, J. Pérez-Juste, S. Bals, G. Van Tendeloo and L. M. Liz-Marzán, J. Phys. Chem. Lett., 2013, 4, 2209-2216.

21. D. E. Sanders and A. E. DePristo, Surface Science, 1992, 260, 116-128.

22. G. S. Ferguson, M. K. Chaudhury, G. B. Sigal and G. M. Whitesides, Science, 1991, 253, 776-778.

23. C. Ji and P. C. Searson, The Journal of Physical Chemistry B, 2003, 107, 4494-4499.

24. W. Ostwald, Z. Phys. Chem., 1897, 289–330.

25. M. Grouchko, P. Roitman, X. Zhu, I. Popov, A. Kamyshny, H. Su and S. Magdassi, Nat. Commun., 2014, 5, 2994.

26. Z. S. Pereira and E. Z. da Silva, The Journal of Physical Chemistry C, 2011, 115, 22870-22876.

27. Y. Lu, J. Y. Huang, C. Wang, S. Sun and J. Lou, Nat. Nanotechnol., 2010, 5, 218-224.

28. D. V. Wagle and G. A. Baker, Materials Horizons, 2015, 2, 157-167.

29. I. Calderon, R. A. Alvarez-Puebla and N. Pazos-Perez, Nanoscale, 2021, 13, 4530-4536.

30. A. Marino-Lopez, M. Blanco-Formoso, L. N. Furini, A. Sousa-Castillo, E. Tiryaki, M. Perez-Lorenzo, M. Testa-Anta, V. Salgueirino, N. A. Kotov, R. A. Alvarez-Puebla and M. A. Correa-Duarte, Langmuir, 2019, 35, 4110-4116.

31. H. Feng, Y. Yang, Y. You, G. Li, J. Guo, T. Yu, Z. Shen, T. Wu and B. Xing, Chemical communications, 2009, 1984-1986.

32. N. Pazos-Pérez, D. Baranov, S. Irsen, M. Hilgendorff, L. M. Liz-Marzán and M. Giersig, Langmuir, 2008, 24, 9855-9860.

33. M. Blanco-Formoso, M. Turino, B. Rivas-Murias, L. Guerrini, A. Shavel, R. de la Rica, M. Correa-Duarte, V. Salgueiriño, N. Pazos-Perez and R. A. Alvarez-Puebla, The Journal of Physical Chemistry C, 2020, 124, 3270-3276.

34. S. Jessl, M. Tebbe, L. Guerrini, A. Fery, R. A. Alvarez-Puebla and N. Pazos-Perez, Small, 2018, 14, 1703879.

35. N. Pazos-Perez, J. M. Fitzgerald, V. Giannini, L. Guerrini and R. A. Alvarez-Puebla, Nanoscale Advances, 2019, 1, 122-131.

36. N. Pazos-Perez, F. J. Garcia de Abajo, A. Fery and R. A. Alvarez-Puebla, Langmuir, 2012, 28, 8909-8914.

37. R.-R. Fang, L.-J. Guo, W. Wang, C.-F. Hou and H. Li, Physics Letters A, 2021, 405, 127425.

38. A. R. Alian, E. Mahdi and S. A. Meguid, Appl. Surf. Sci., 2020, 507, 145183.

39. Y. Liu, J. Zhang, H. Gao, Y. Wang, Q. Liu, S. Huang, C. F. Guo and Z. Ren, Nano Lett., 2017, 17, 1090-1096.

40. S. Bettscheider, T. Kraus and N. A. Fleck, Acta Mater., 2022, 231, 117799.

41. Y. Q. Wang, W. S. Liang and C. Y. Geng, Nanoscale Research Letters, 2009, 4, 684.

42. S.-H. Cha, Y. Park, J. W. Han, K. Kim, H.-S. Kim, H.-L. Jang and S. Cho, Sci. Rep., 2016, 6, 32951.

43. T. Toshihiro and M. Shigetoshi, Bulletin of the Chemical Society of Japan, 1990, 63, 533-537.

44. E. Carbó-Argibay, B. Rodríguez-González, I. Pastoriza-Santos, J. Pérez-Juste and L. M. Liz-Marzán, Nanoscale, 2010, 2, 2377-2383.

45. C. J. Johnson, E. Dujardin, S. A. Davis, C. J. Murphy and S. Mann, Journal of Materials Chemistry, 2002, 12, 1765-1770.

46. R. Holze, Phys. Chem. Chem. Phys., 2015, 17, 21364-21372.

47. S. Pande, S. K. Ghosh, S. Praharaj, S. Panigrahi, S. Basu, S. Jana, A. Pal, T. Tsukuda and T. Pal, J. Phys. Chem. C, 2007, 111, 10806-10813.

48. Y. J. Li, Q. R. Shi, P. N. Zhang, Y. J. Xiahou, S. Z. Li, D. Y. Wang and H. B. Xia, J. Mater. Chem. C, 2016, 4.

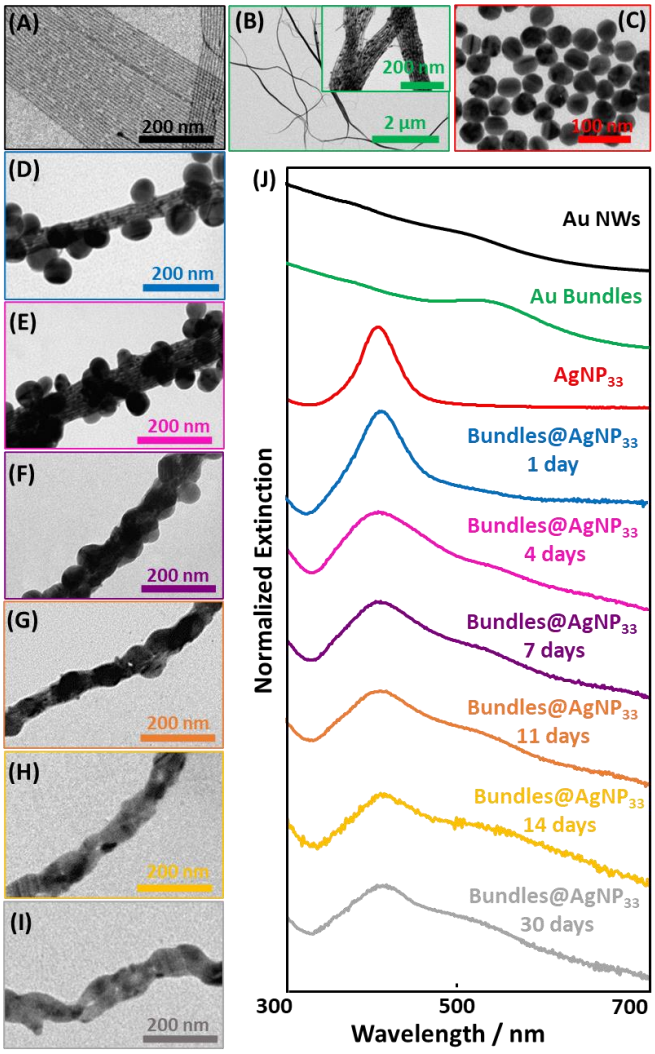

Fig. 1 (A-C) Representative TEM images of the initial components of the assemblies (A) ultrathin gold nanowires (AuNWs), (B) bundles of gold nanowires, and (C) silver nanoparticles of 33 ± 3 nm diameter ($AgNP_{33}$). (D-I) Representative TEM images of the bundle@$AgNP_{33}$ assemblies at different stages of the welding process (1, 4, 7, 11, 14 and 30 days, from D to I, respectively). (J) Extinction spectra of individual AuNWs, Au bundles and $AgNP_{33}$ suspensions, and the bundle@$AgNP_{33}$ assemblies over time. The intensity of the stacked extinction spectra was adjusted for better visualization.

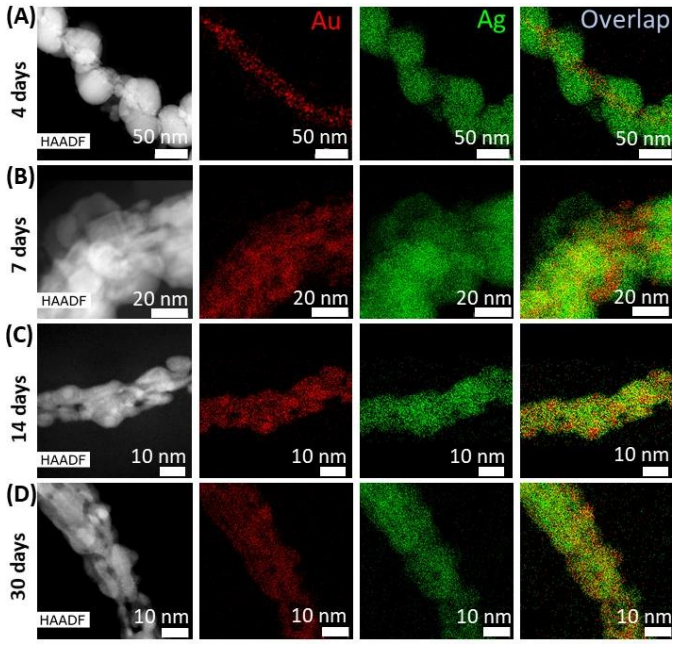

Fig. 2 (A-D) Representative high-angle annular dark-field scanning transmission electron microscopy (HAADF-STEM) images of the bundle@$AgNP_{33}$ welding process at different stages (4, 7, 14 and 30 days). The images shown on the right of the figure are the corresponding elemental maps for Au and Ag (individual and overlapped) obtained via EDX analysis of the STEM images (A-D).

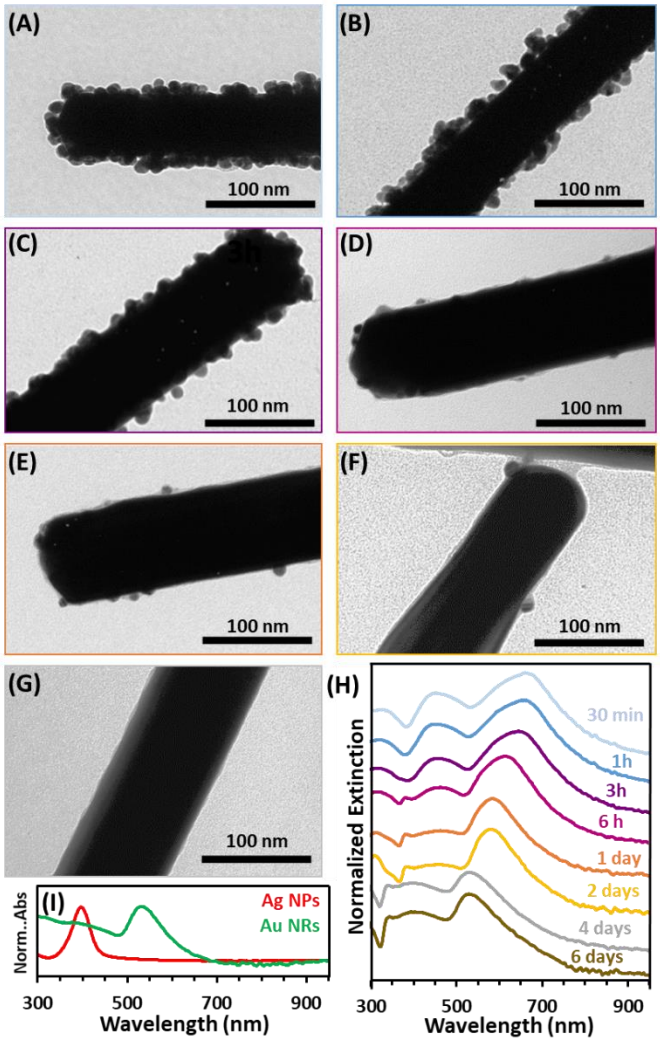

Fig. 3 (A-G) Representative TEM images of NR@$AgNP_{15}$ assemblies at 7 different stages of the welding process (30 min, 1 h, 3 h, 6 h, 1 day, 2 days, and 4 days). (H) Extinction spectra of the assemblies over 6 days. (I) Extinction spectra of the individual AuNRs and $AgNP_{15}$ colloids. The stacked extinction spectra were normalized to their maxima for better visualization.

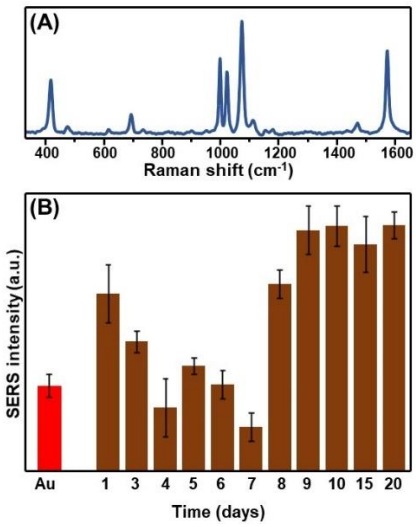

Fig. 5 (A) SERS spectrum of benzenethiol (BT) on $AuNP_{107}$@$AgNP_{15}$ assemblies (day 1, 785 nm laser). (B) SERS intensities of the 1070 cm^{-1} BT bands acquired at different stages of the welding process (N = 20). The SERS intensity of $AuNP_{100}$ alone was also included. $AgNP_{15}$ particles did not provide any distinguishable signal.

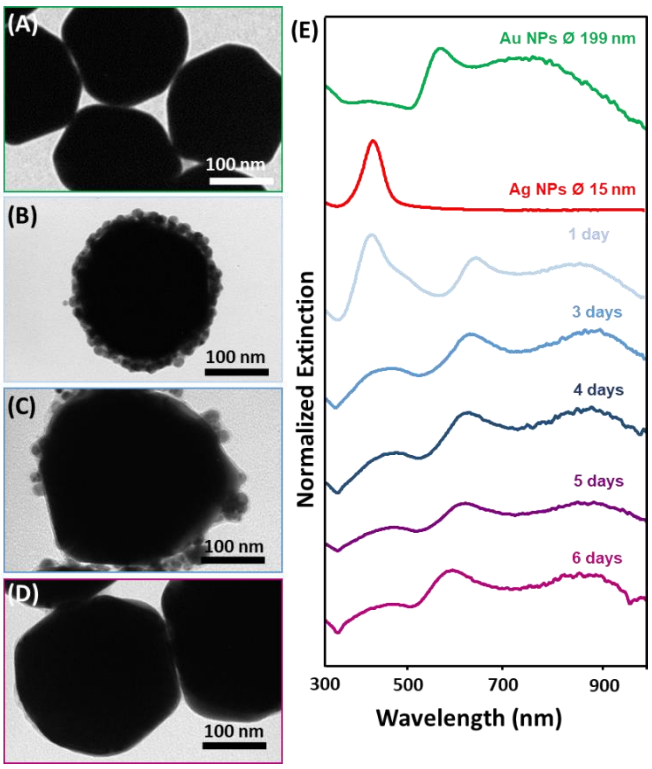

Fig. 6. (A) Representative TEM image of ca. 199 nm AuNPs. (B-D) TEM images the AuNPs shown in (A) coated with 15 nm AgNPs at 3 stages during the welding process (1, 3, and 6 days from (B) to (D) respectively). (E) Extinction spectra corresponding to 5 different stages of welding. The spectra of the initial Au and AgNPs before the assembling are also included.

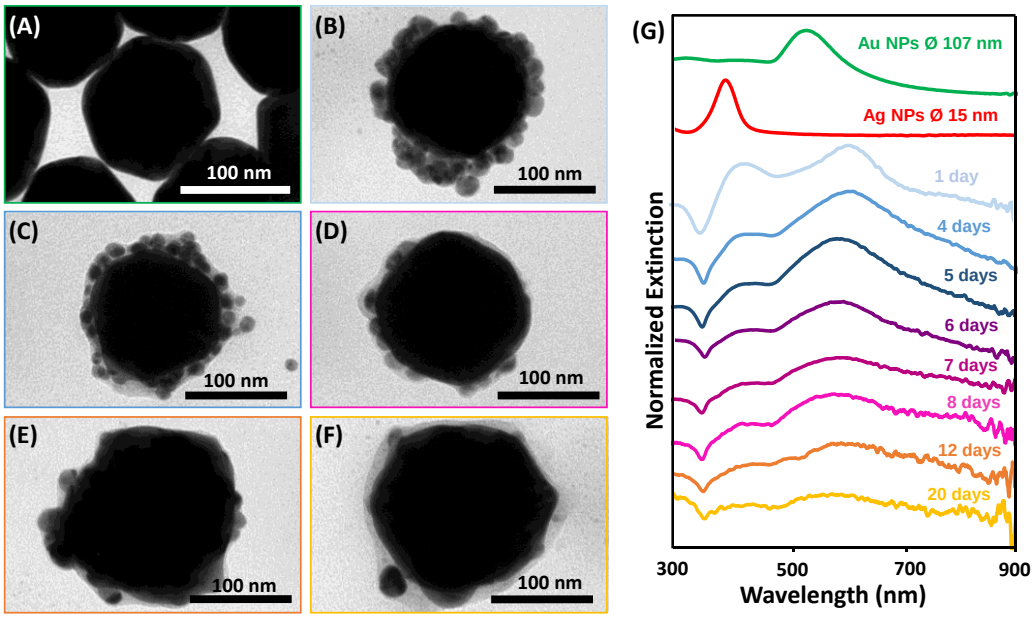

Fig. 4 (A) Representative TEM image of approx. 107 nm Au nanoparticles ($AuNP_{107}$). (B-F) Representative TEM images the $AuNP_{107}$@$AgNP_{15}$ assemblies at 5 different stages of the welding process (1, 4, 8, 12, and 20 days, from (B) to (F) respectively). (G) Extinction spectra of the $AuNP_{107}$@$AgNP_{15}$ assemblies over a period of 20 days. The initial spectra of the individual Au and Ag colloids were also included. The stacked extinction spectra were normalized to their maxima for better visualization.